Recozimento

Energia armazenada na deformação plástica

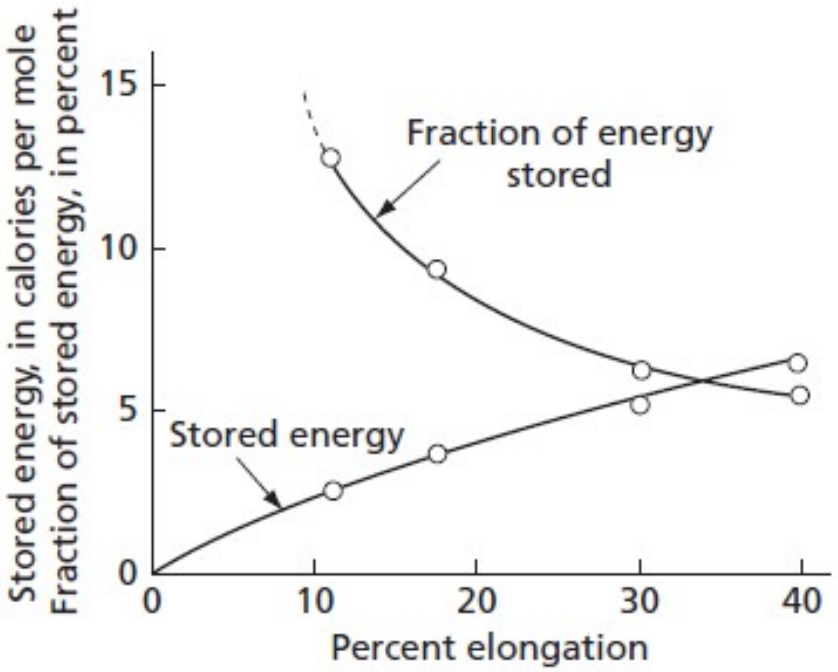

FIG. 8.1 Stored energy of cold work and fraction of the total work of deformation remaining as stored energy for high purity copper plotted as functions of tensile elongation. (Data of Gordon, P., *Trans. AIME*, **203** 1043 (1955).)

Liberação da energia armazenada

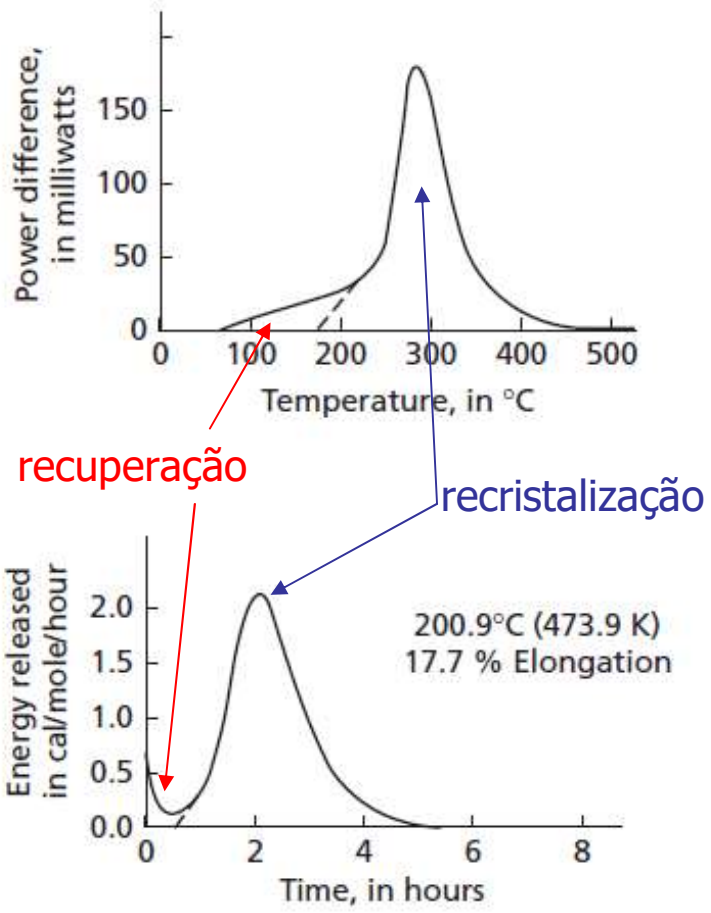

FIG. 8.2 Anisothermal anneal curve. Electrolytic copper. (From Clarebrough, H. M., Hargreaves, M.E., and West, G.W., *Proc. Roy. Soc.*, London, **232A**, 252 (1955).)

FIG. 8.3 Isothermal anneal curve. High purity copper. (From data of Gordon, P., *Trans. AIME*, **203** 1043 (1955).)

Evolução da microestrutura

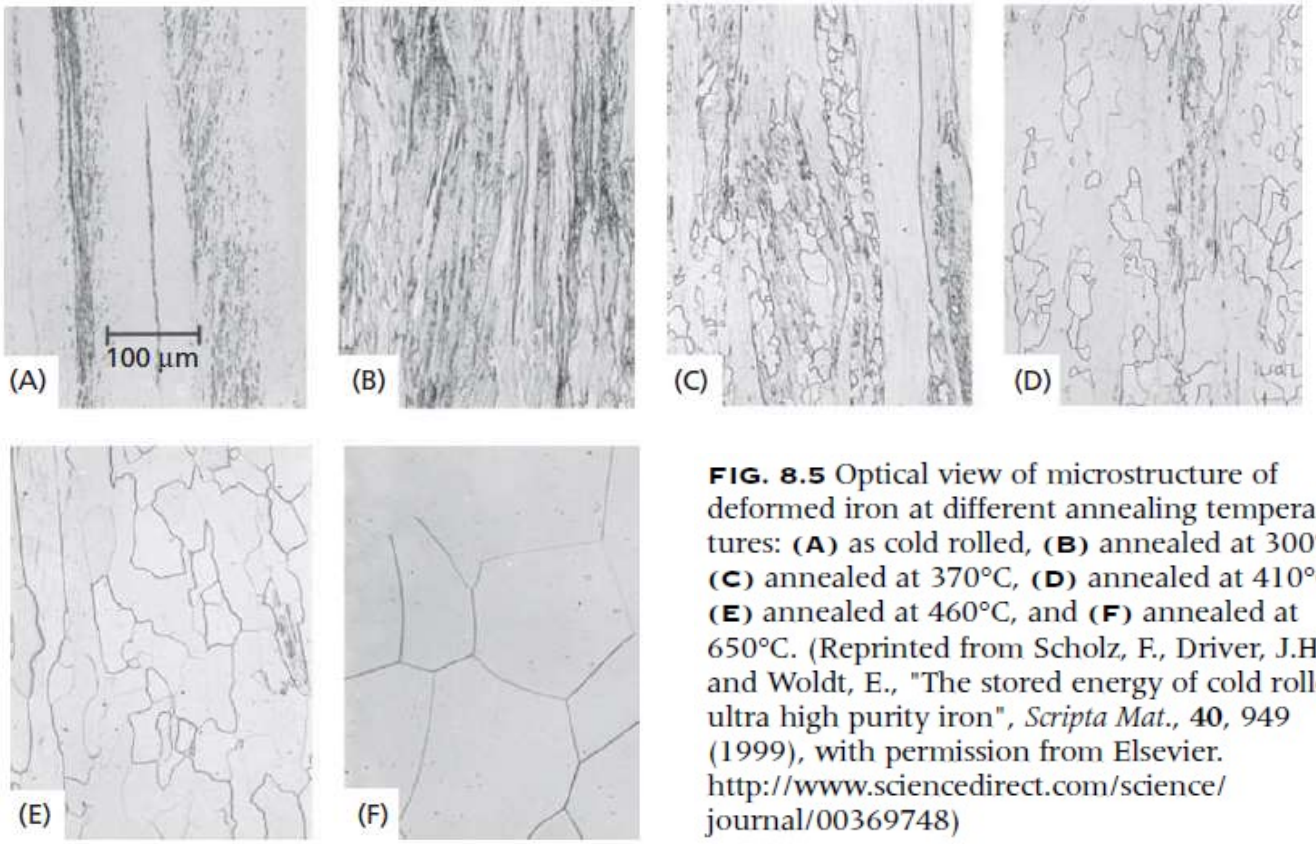

FIG. 8.5 Optical view of microstructure of deformed iron at different annealing temperatures: **(A)** as cold rolled, **(B)** annealed at 300°C, **(C)** annealed at 370°C, **(D)** annealed at 410°C, **(E)** annealed at 460°C, and **(F)** annealed at 650°C. (Reprinted from Scholz, F., Driver, J.H., and Woldt, E., "The stored energy of cold rolled ultra high purity iron", *Scripta Mat.*, **40**, 949 (1999), with permission from Elsevier. http://www.sciencedirect.com/science/journal/00369748)

Recuperação

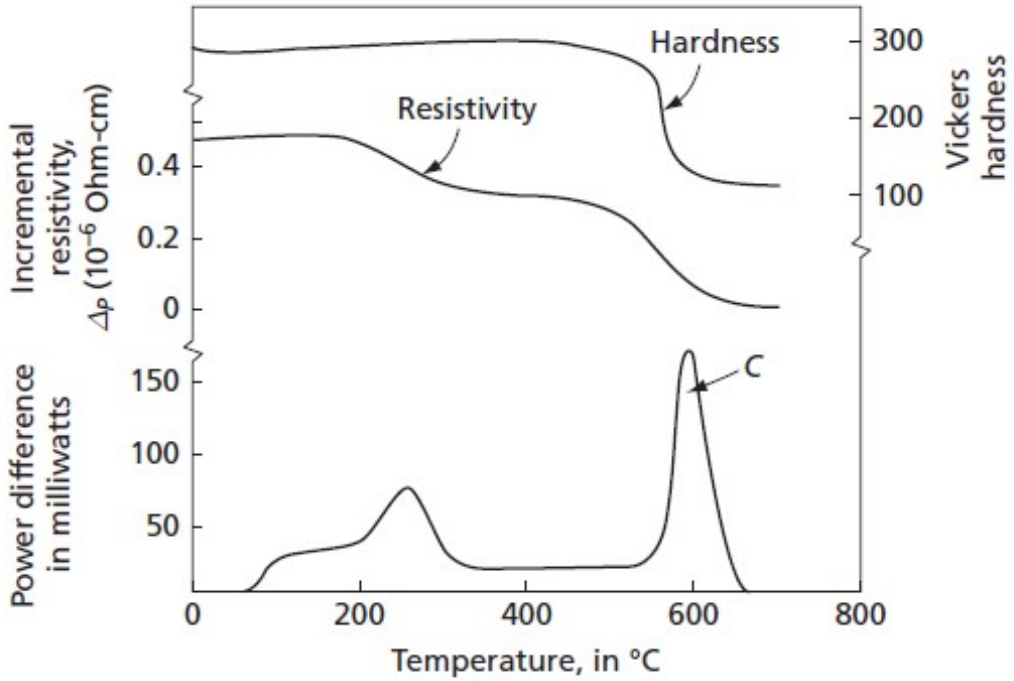

FIG. 8.6 Anisothermal-anneal curve for cold-worked nickel. At the top of the figure curves are also drawn to show the effect of annealing temperature on the hardness and incremental resistivity of the metal. (From Clarebrough, H.M., Hargreaves, M.E., and West, G.W., *Proc. Roy. Soc.*, London, **232A**, 252 (1955).)

Recuperação em monocristais

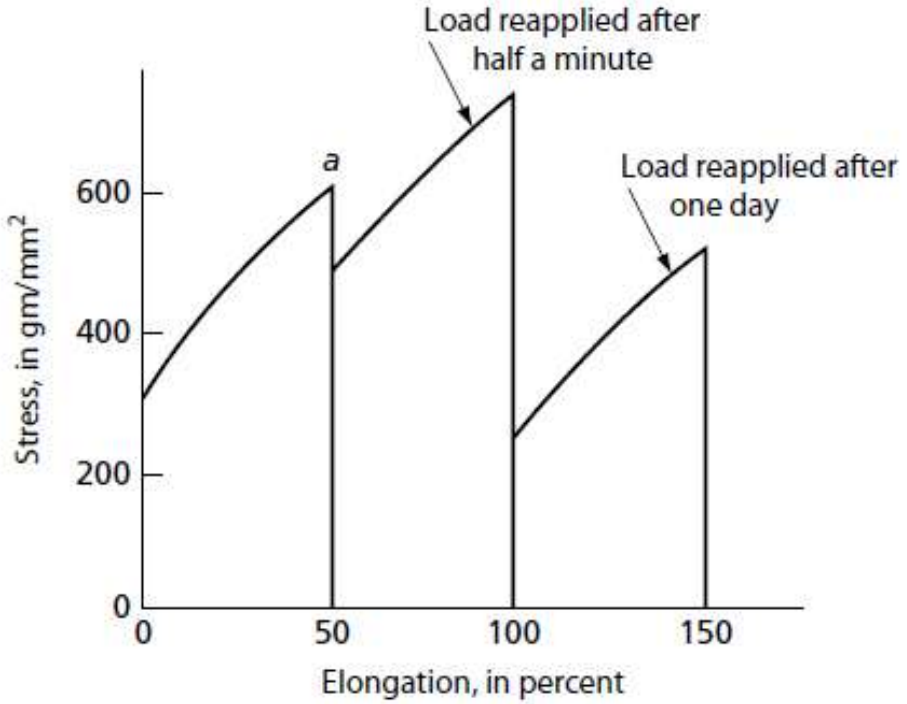

FIG. 8.7 Recovery of the yield strength of a zinc single crystal at room temperature. (After Schmid, E., and Boas, W., *Kristallplastizität*, Julius Springer, Berlin, 1935.)

Recuperação em monocristais

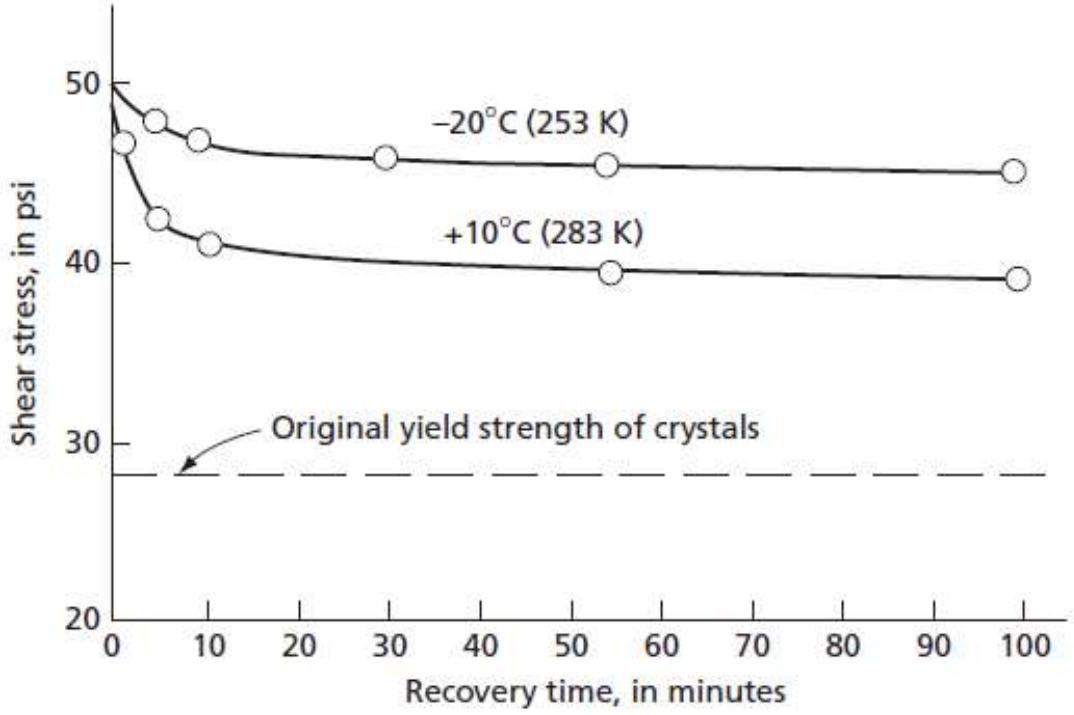

FIG. 8.8 Recovery of the yield strength of zinc single crystals at two different temperatures. (From the data of Drouard, R., Washburn, J., and Parker, E. R., *Trans. AIME*, **197** 1226 [1953].)

$$\frac{1}{\tau} = Ae^{-Q/RT}$$

$$\frac{\tau_1}{\tau_2} = \frac{e^{-Q/RT_2}}{e^{-Q/RT_1}} = e^{-\frac{Q}{R}\left(\frac{1}{T_2}-\frac{1}{T_1}\right)}$$

Poligonização

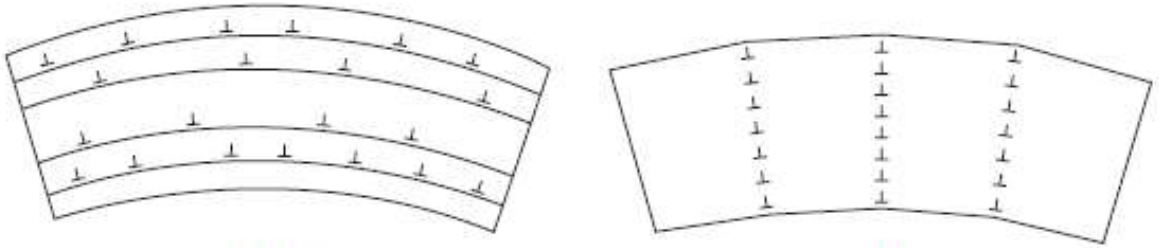

FIG. 8.10 Realignment of edge dislocations during polygonization **(A)** The excess dislocations that remain on active slip planes after a crystal is bent. **(B)** The rearrangement of the dislocations after polygonization

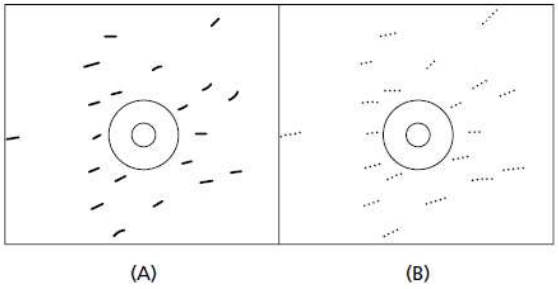

FIG. 8.9 Schematic Laue patterns showing how polygonization breaks up asterated X-ray reflections into a series of discrete spots. The diagram on the left corresponds to reflections from a bent single crystal; that on the right corresponds to the same crystal after an anneal that has polygonized the crystal

Rearranjo das discordâncias

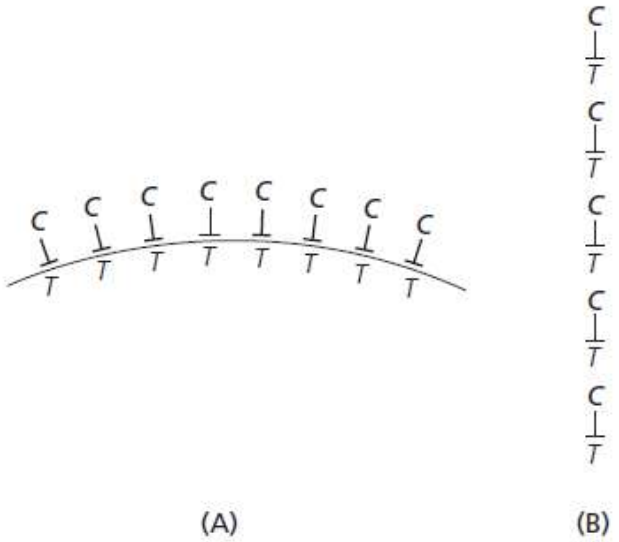

FIG. 8.11 Simple explanation showing why a vertical array of edge dislocations corresponds to a lower state of strain energy than does an array of the same dislocations, all on a single slip plane. The letters *T* and *C* in **(A)** and **(B)** correspond to the tensile and compressive strains associated with each dislocation

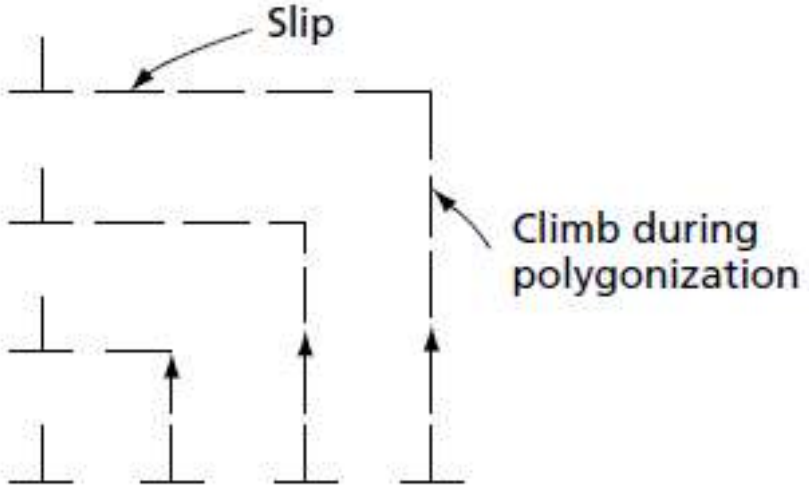

FIG. 8.12 Both climb and slip are involved in the rearrangement of edge dislocations

Rearranjo de discordâncias

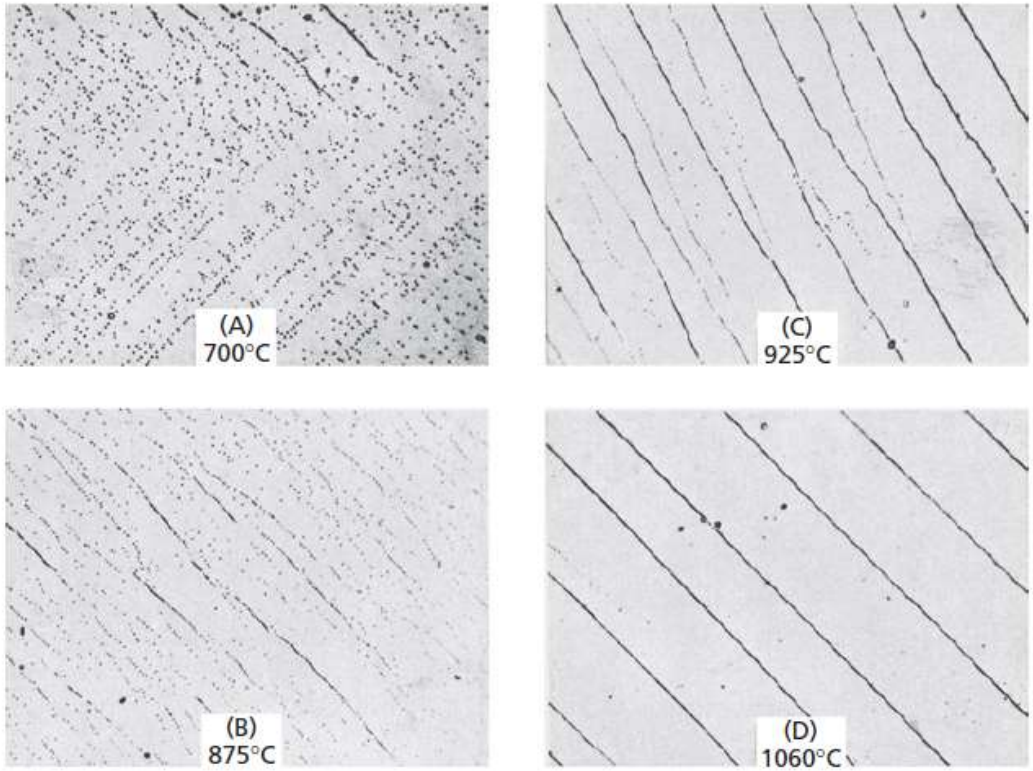

FIG. 8.14 Polygonization in bent and annealed iron-silicon single crystals. All specimens annealed for one hour at the indicated temperatures. Note that polygonization is more complete the higher the temperature of the anneal. All pictures were taken at 750×. (Reprinted from Hibbard, W.R. Jr, and Dunn, C.G., "A study of <112> edge dislocations in bent silicone-iron single crystals", *Acta Met.* 4 306 (1956), fig. 11, 14, 16 and 19 with permission of Elsevier. www.sciencedirect.com/science/journal/00016160.)

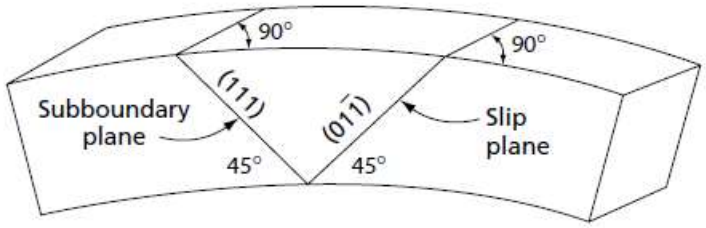

FIG. 8.13 Orientation of the iron-silicon crystal shown in the photographs of Fig. 8.14

Formação de subgrãos

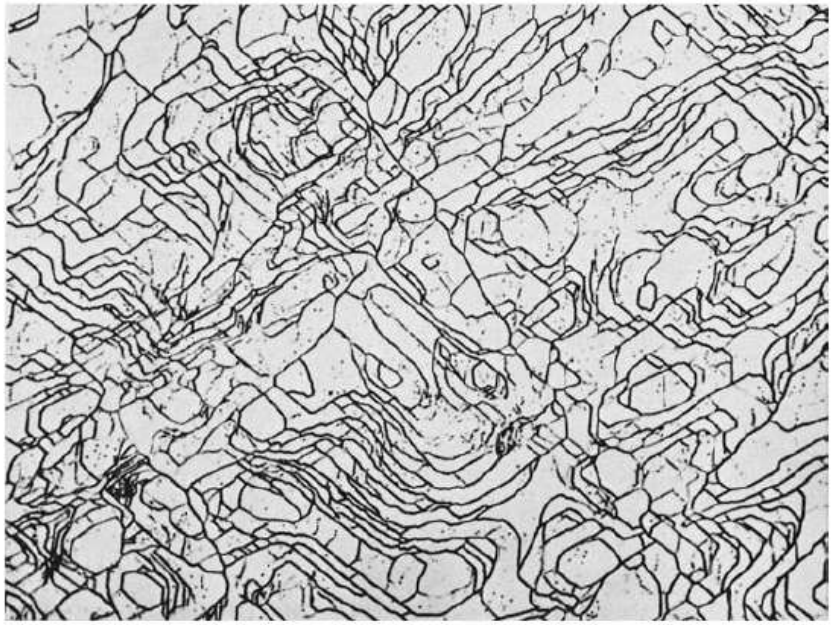

FIG. 8.15 Complex polygonized structure in a silicon-iron single crystal that was formed 8 percent by cold rolling before it was annealed 1 hr at 1373 K. (From Hibbard, W.R. Jr, and Dunn, ASM Seminar, *Creep and Recovery*, 1957, p. 52 Reprinted with permission of ASM International(R). All rights reserved. www.asminternational.org)

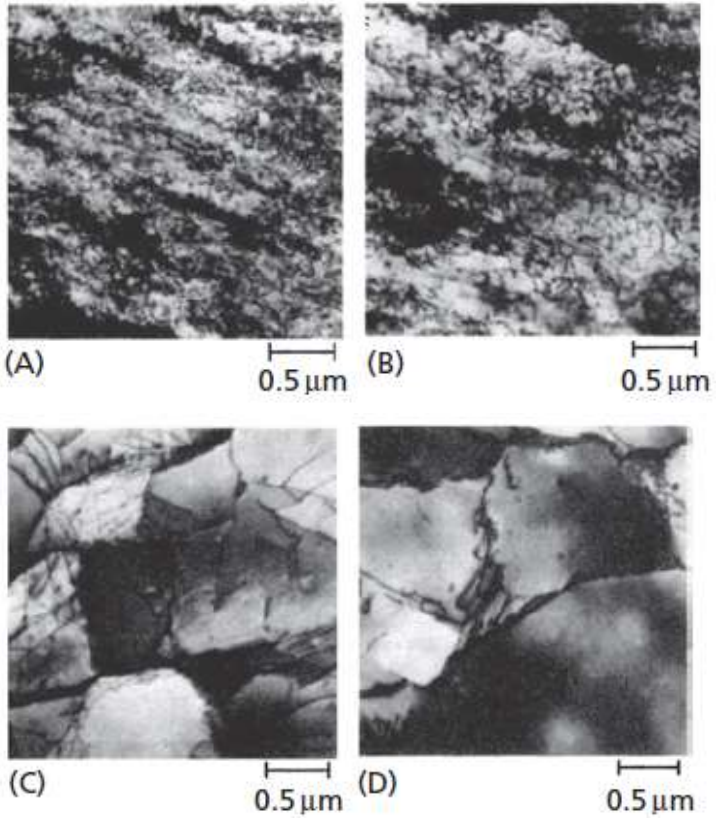

FIG. 8.16 Effect of annealing time and temperature on the microstructure of iron–3% Si single crystal cold rolled in the (00!) [100] orientation. (From Metallurgy and Microstructures, *ASM handbook*, published by ASM International, 2004, page 209. Reprinted with permission of ASM International(R). All rights reserved. www.asminternational.org)

Tempo e temperatura na recristalização

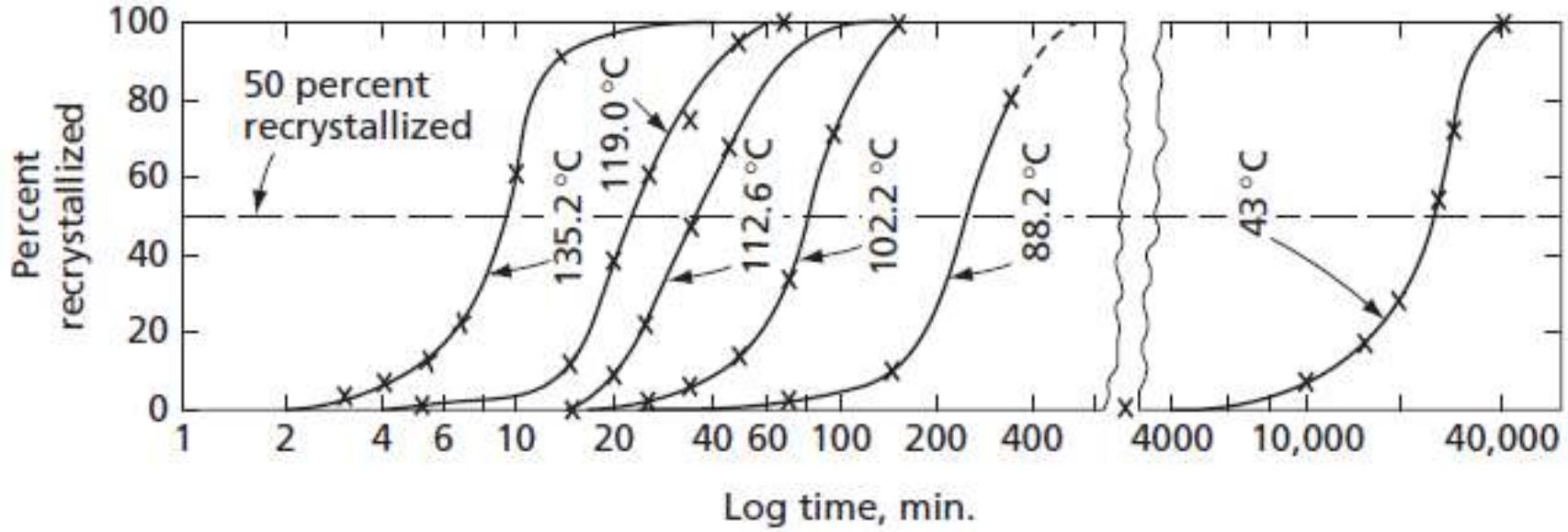

FIG. 8.17 Isothermal transformation (recrystallization) curves for pure copper (99.999 percent Cu) cold-rolled 98 percent. (From Decker, B. F., and Harker, D., *Trans. AIME*, **188** 887 [1950].)

Tempo e temperatura na recristalização

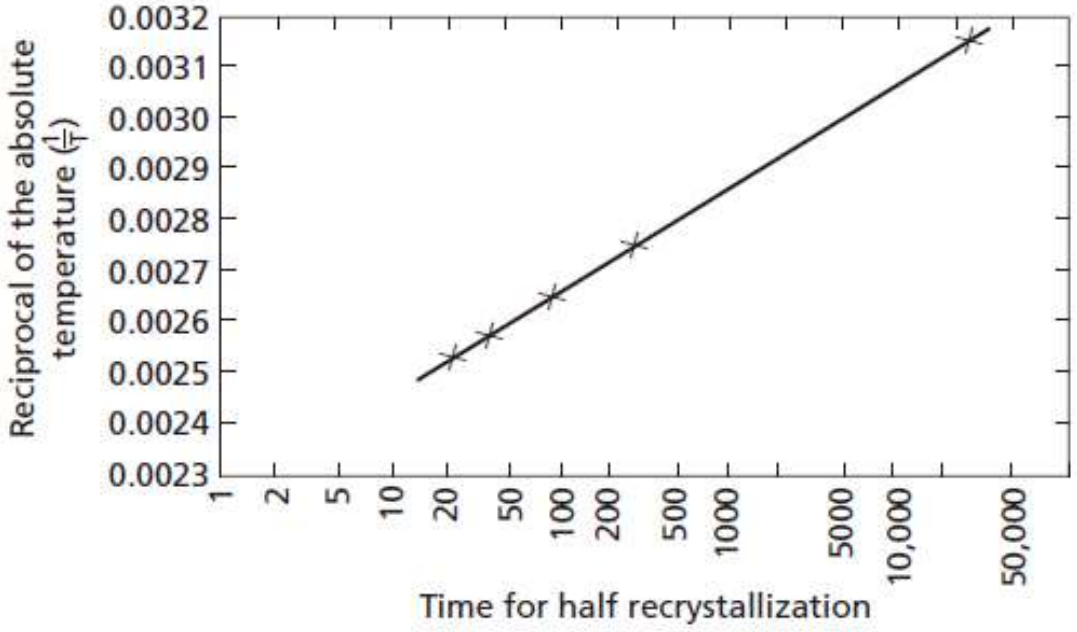

FIG. 8.18 Reciprocal of absolute temperature (K) vs. time for half recrystallization of pure copper. (From Decker, B. F., and Harker, D., *Trans. AIME*, **188** [1950].)

$$\frac{1}{T} = K \log_{10} \frac{1}{\tau} + C$$

$$\frac{1}{\tau} = Ae^{-Q_r/RT}$$

Explicar T de recristalização

A deformação e a energia de ativação para a recristalização

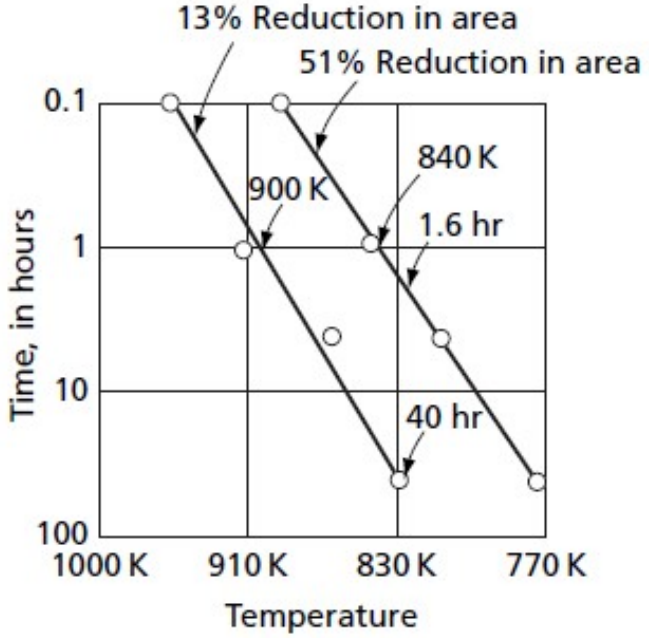

FIG. 8.19 Temperature-time relationships for recrystallization of zirconium (iodide) corresponding to two different amounts of prior cold work. (Treco, R. M., Proc., 1956, *AIME* Regional Conference on Reactive Metals, p. 136.)

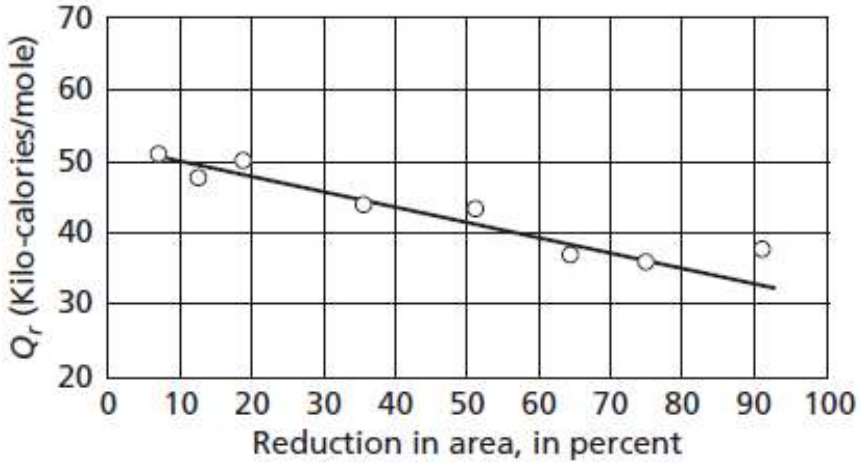

FIG. 8.20 Activation energy for the recrystallization of zirconium (iodide) as a function of the amount of cold work. (Treco, R. M., Proc., 1956, *AIME* Regional Conference on Reactive Metals, p. 136.)

Nucleação

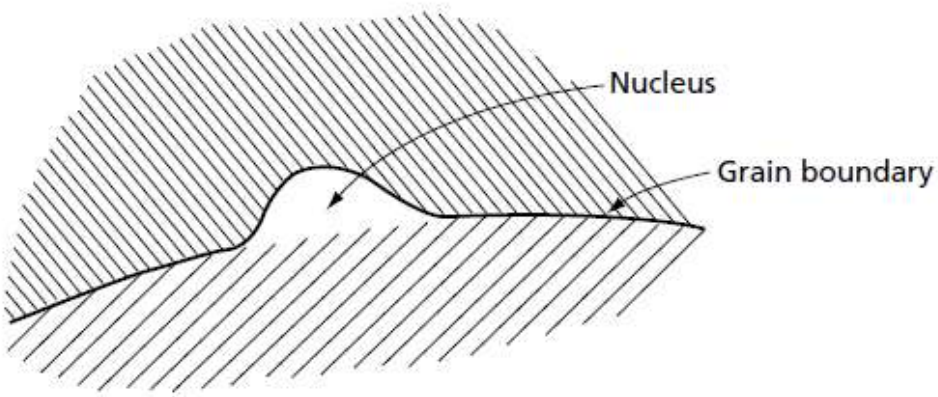

FIG. 8.21 The bulge mechanism for the formation of a nucleus at a grain boundary. (After Bailey, J.E., and Hirsh, P.B., *Proc. Roy Soc.*, **A267**, 11 (1962).)

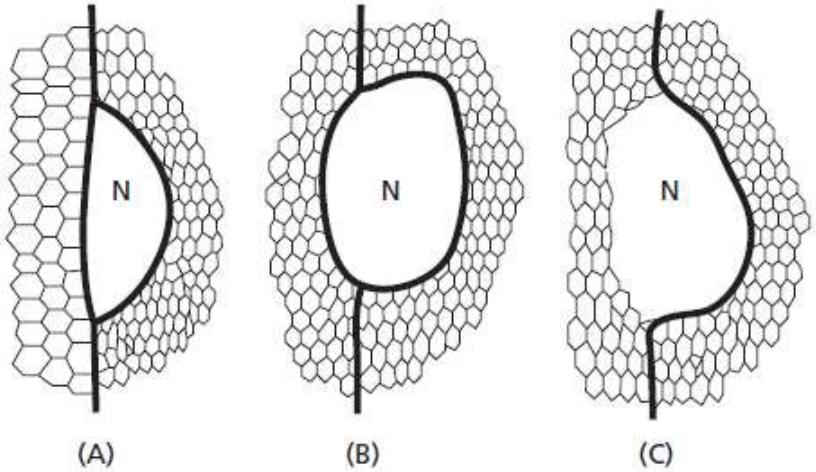

FIG. 8.22 Schematic drawing of grain boundary nuclei, marked by N, between two deformed grains with hexagonal subgrains. (From Ray, B. and Hansen, N., *Met. Trans. A*, **15A** 293 (1984) with kind permission of Springer Science and Business Media.)

Tamanho de grão após a recristalização

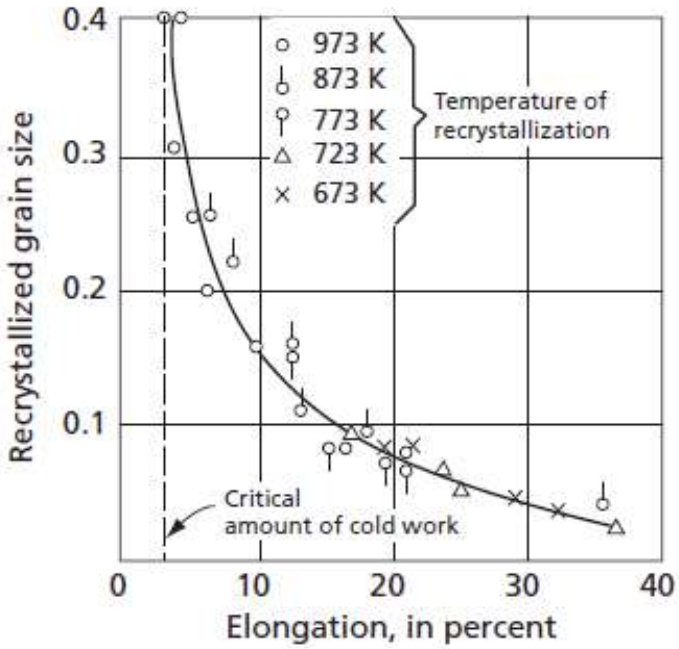

FIG. 8.23 Effect of prior cold work on the recrystallized grain size of alpha-brass. Notice that the grain size at the end of recrystallization does not depend on the temperature of recrystallization. (Smart, J. S., and Smith, A. A., *Trans. AIME*, **152** 103 [1943].)

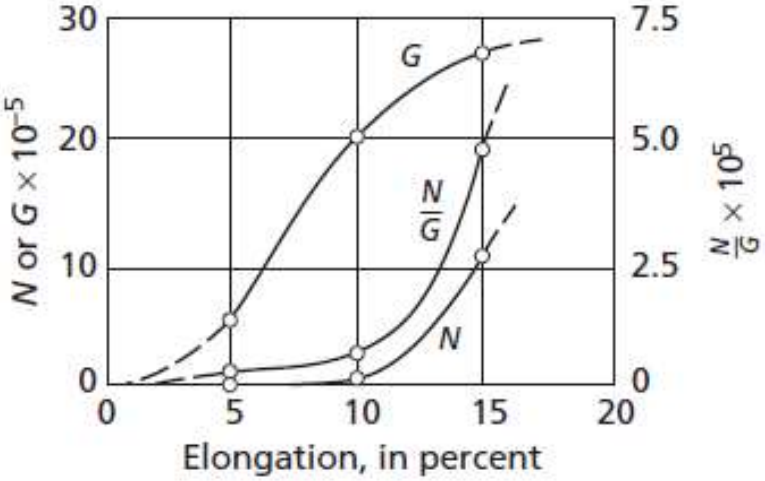

FIG. 8.24 Variation of the rate of nucleation (N), the rate of growth (G), and their ratio (N/G) as a function of deformation before annealing. (Data for aluminum annealed at 350°C.) (From Anderson, W. A., and Mehl, R. F., *Trans. AIME*, **161** 140 [1945].)

Efeito de impurezas

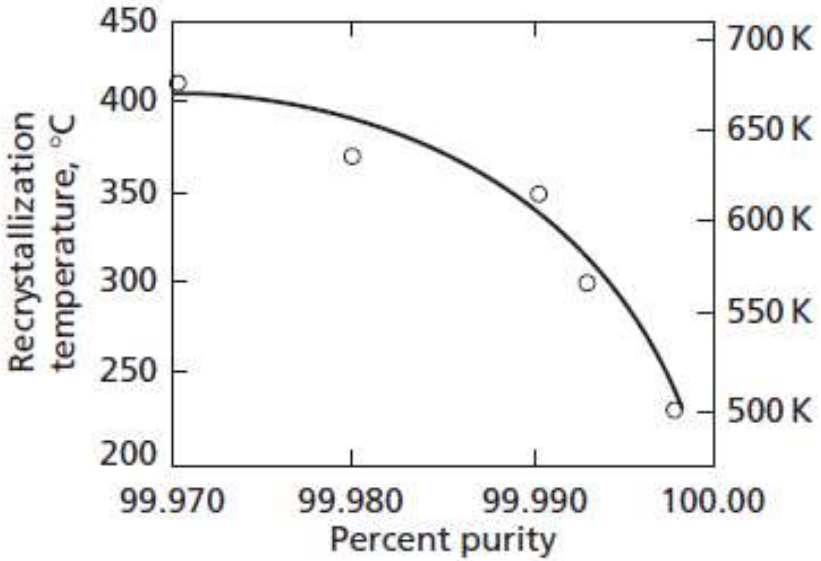

FIG. 8.25 Effect of impurities on the recrystallization temperature (30 minutes of annealing) of aluminum cold-rolled 80 percent. (From Perryman, E.C.W., ASM Seminar, *Creep and Recovery*, 1957, p. 111. Reprinted with permission of ASM International(R). All rights reserved. www.asminternational.org)

TABLE 8.1 Increase in the Recrystallization Temperature of Pure Copper by the Addition of 0.01 Atomic Percent of the Indicated Element.*

Added Element	Increase in Recrystallization Temperature K
Ni	0
Co	15
Fe	15
Ag	80
Sn	180
Te	240

*Data of Smart, J. S., and Smith, A. A., *Trans. AIME*, **147** 48 (1942); **166** 144 (1946).

Crescimento de grão

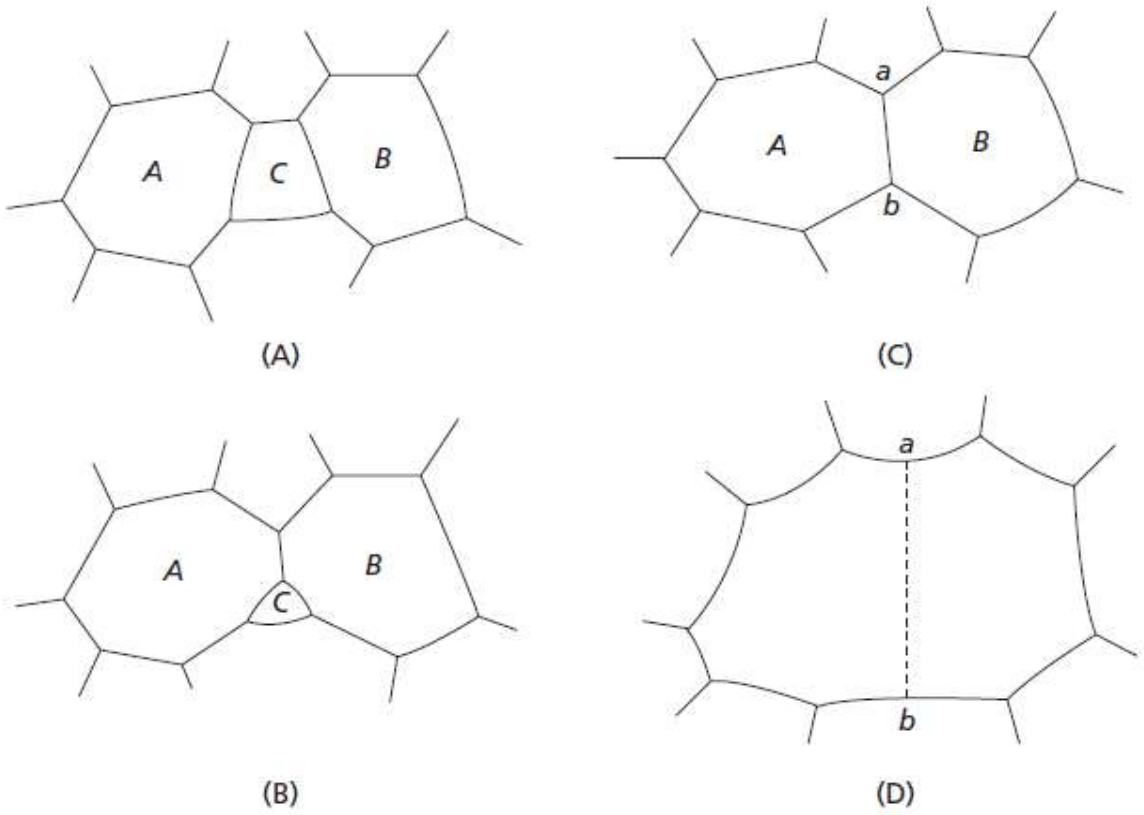

FIG. 8.29 Geometrical coalescence. Two grains, *A* and *B*, encounter as a result of the disappearance of grain *C*. If grains *A* and *B* have nearly identical orientation, then boundary *ab* becomes the equivalent of a subboundary and grains *A* and *B* may be considered the equivalent of a single grain

A equação do crescimento

$$\frac{D^2 - D_0^2}{t} = K_0 e^{-Q/RT}$$

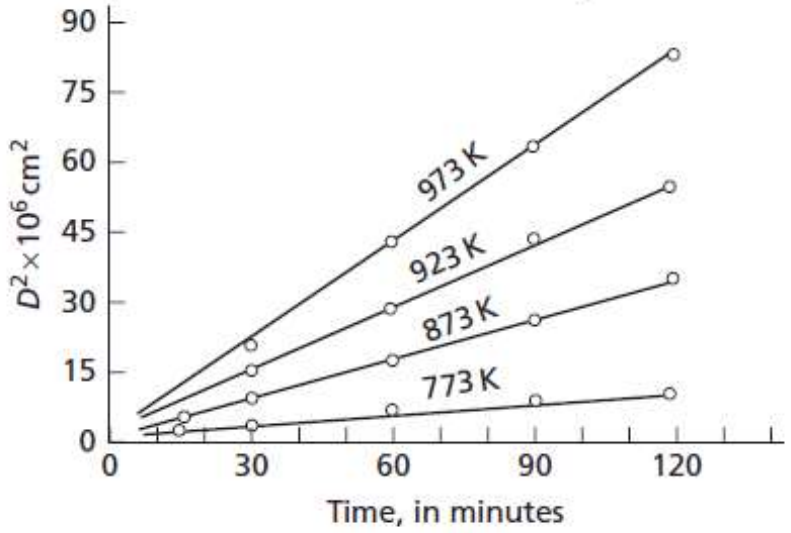

FIG. 8.32 Grain-growth isotherms for alpha-brass (10 percent Zn–90 percent Cu). Notice that the grain diameter squared (D^2) varies directly as the time. (Reprinted from Feltham, P., and Copley, G.J., "Grain-growth in a brasses", *Acta Met.*, **6** 539 (1958) with permission from Elsevier. www.sciencedirect.com/science/journal/00016160)

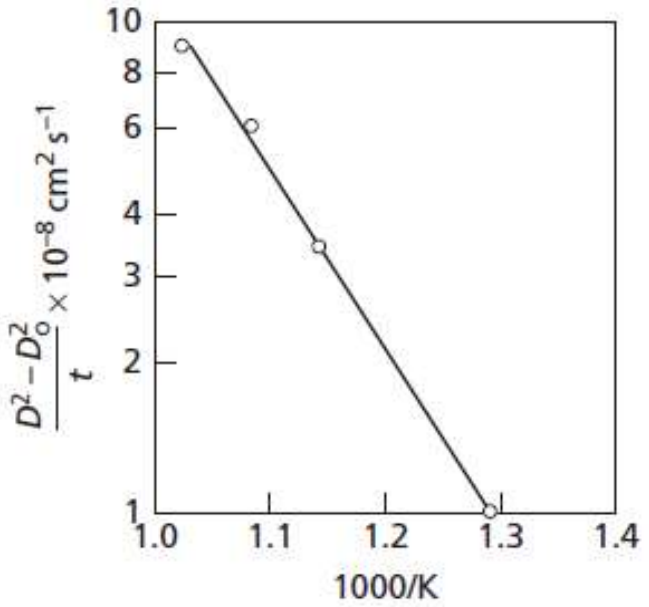

FIG. 8.33 The logarithms of the slope of the isotherms of Fig. 8.32 vary directly as the reciprocal of the absolute temperature. (Reprinted from Feltham, P., and Copley, G.J., "Grain-growth in a brasses", *Acta Met.*, **6** 539 (1958) with permission from Elsevier. www.sciencedirect.com/science/journal/00016160)

Efeito de solução sólida

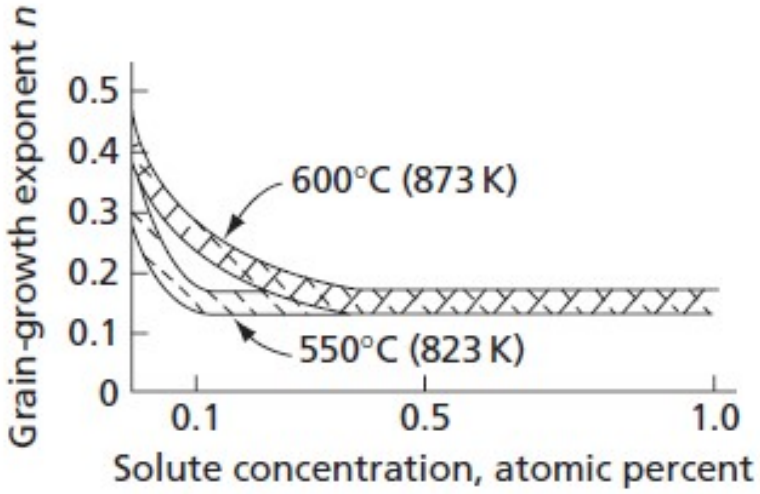

FIG. 8.34 Variation of the grain-growth exponent of copper with the concentration of aluminum in solid solution. (From Weinig, S., and Machlin, E. S., *Trans. AIME*, **209** 843 [1957].)

Efeito de inclusões

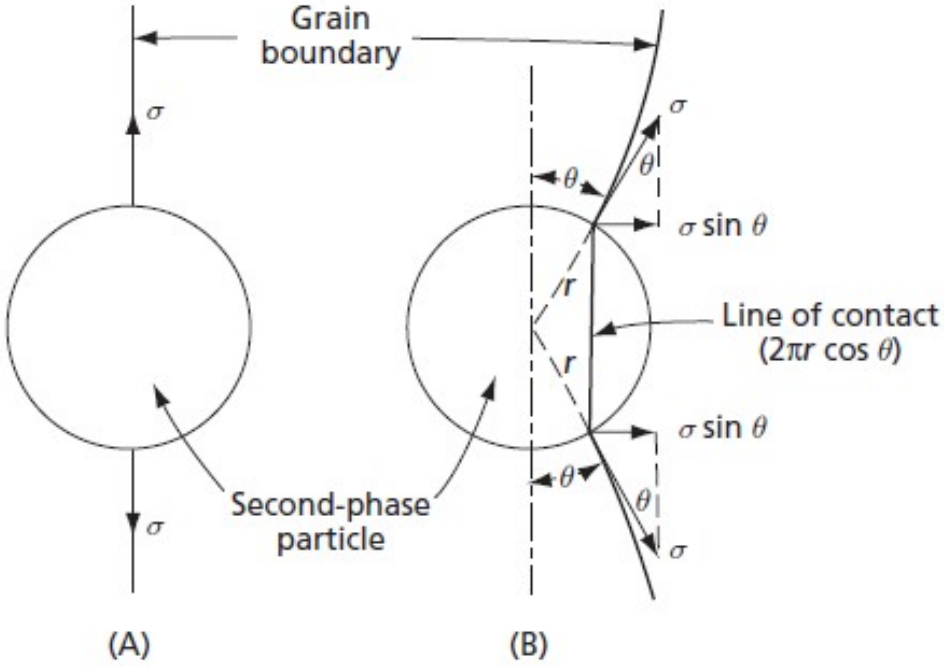

FIG. 8.35 Interaction between a grain boundary and a second-phase inclusion

$$f = 2\pi r\sigma \cos\theta \sin\theta$$

$$f = \pi r\sigma$$

Efeito de inclusões

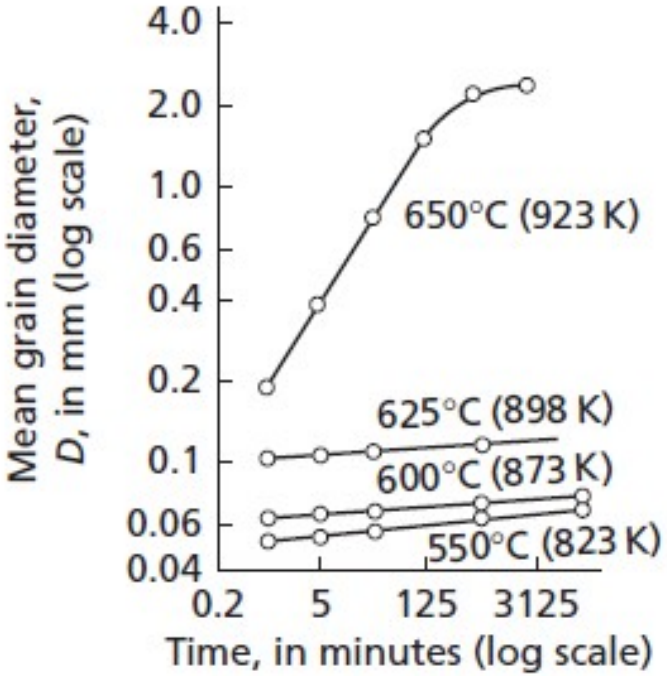

FIG. 8.36 The effect of second-phase inclusions on grain growth in a manganese-aluminum alloy (1.1 percent Mn). Grain growth is severely inhibited at the temperatures below 923 K because of the presence of second-phase precipitate particles ($MnAl_6$). (From Beck, P. A., Holzworth, M. L., and Sperry, P., *Trans. AIME*, **180** 163 [1949].)

Relação de Zener: $R = \frac{4}{3}\frac{r}{\zeta}$

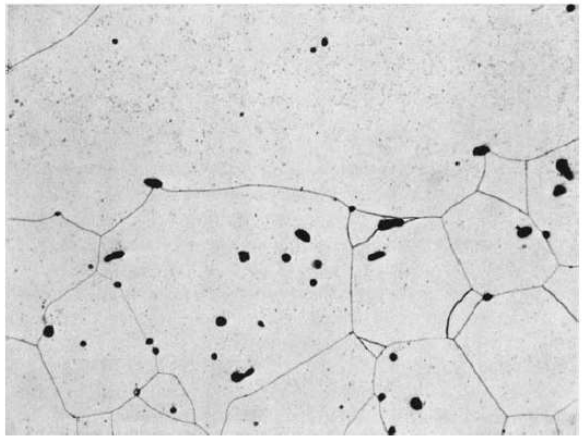

FIG. 8.37 Interaction between pores and grain boundaries

Efeito da superfície

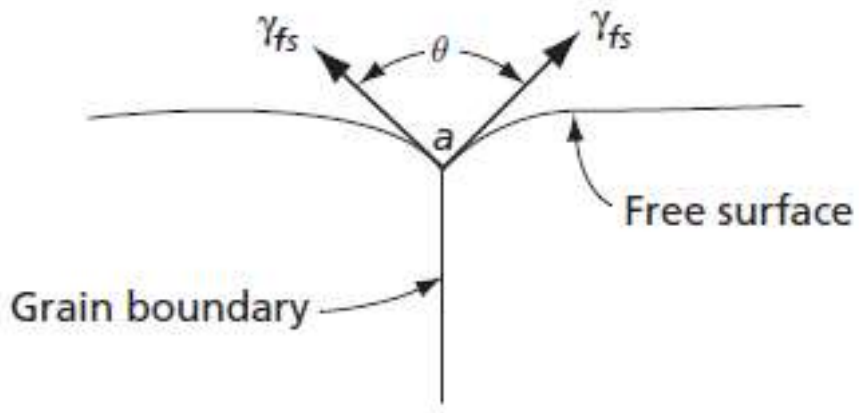

FIG. 8.38 A thermal groove

$$\gamma_b = 2\gamma_{\text{f.s.}} \cos\frac{\theta}{2}$$

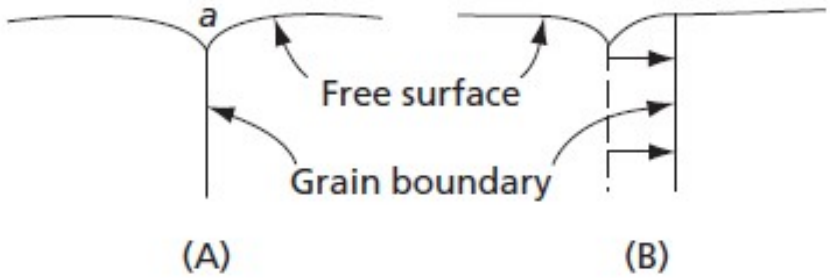

FIG. 8.39 Moving a grain boundary away from its groove increases its surface if the boundary is nearly normal to the free surface

Tamanho limite

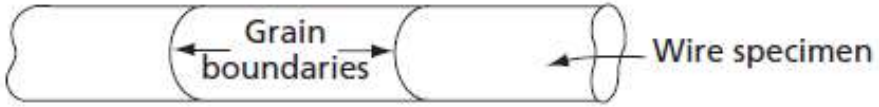

FIG. 8.40 One example of a stable grain-boundary configuration

Relação de Zener: $R = \frac{4}{3}\frac{r}{\zeta}$

p/ o caso de limitação devido à presença de inclusões

Recristalização secundária

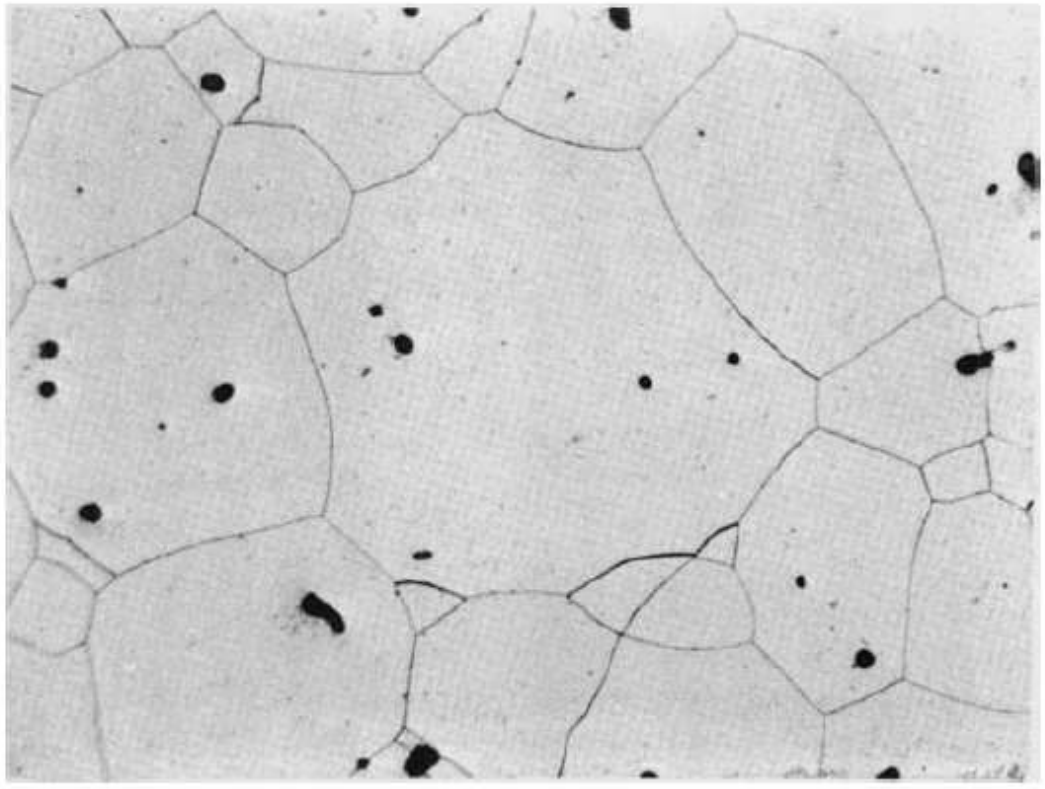

FIG. 8.41 A specimen undergoing secondary recrystallization. Notice that the central grain has thirteen sides